J. Fluid Mech. (2010), *vol.* 662, *pp.* 209–231. © Cambridge University Press 2010
doi:10.1017/S0022112010003149

On the lateral migration of a slightly deformed bubble rising near a vertical plane wall

KAZUYASU SUGIYAMA[1]† AND FUMIO TAKEMURA[1,2]

[1]Department of Mechanical Engineering, School of Engineering, The University of Tokyo, 7-3-1 Hongo, Bunkyo-ku, Tokyo 113-8656, Japan

[2]National Institute of Advanced Industrial Science and Technology, 1-2-1 Namiki, Tsukuba, Ibaraki 305-8564, Japan

(Received 22 March 2009; revised 8 June 2010; accepted 8 June 2010; first published online 18 August 2010)

Deformation-induced lateral migration of a bubble slowly rising near a vertical plane wall in a stagnant liquid is numerically and theoretically investigated. In particular, our focus is set on a situation with a short clearance c between the bubble interface and the wall. Motivated by the fact that numerically and experimentally measured migration velocities are considerably higher than the velocity estimated by the available analytical solution using the Faxén mirror image technique for $a/(a+c) \ll 1$ (here a is the bubble radius), when the clearance parameter $\varepsilon(=c/a)$ is comparable to or smaller than unity, the numerical analysis based on the boundary-fitted finite-difference approach solving the Stokes equation is performed to complement the experiment. The migration velocity is found to be more affected by the high-order deformation modes with decreasing ε. The numerical simulations are compared with a theoretical migration velocity obtained from a lubrication study of a nearly spherical drop, which describes the role of the squeezing flow within the bubble–wall gap. The numerical and lubrication analyses consistently demonstrate that when $\varepsilon \leqslant 1$, the lubrication effect makes the migration velocity asymptotically $\mu V_{B1}^2/(25\varepsilon\gamma)$ (here, V_{B1}, μ and γ denote the rising velocity, the dynamic viscosity of liquid and the surface tension, respectively).

Key words: drops and bubbles, lubrication theory, Stokesian dynamics

1. Introduction

Recent technical progress in generating microbubbles (e.g. Garstecki *et al.* 2006; Makuta *et al.* 2006), including potentials as actuator and sensor, has enhanced the range of applications, e.g. additives to reduce turbulence friction (Serizawa *et al.* 2005), drug delivery capsules (Shortencarier *et al.* 2004) and contrast agents (Correas *et al.* 2001). In many situations, a bubble encounters a boundary wall during its transport process, and a hydrodynamic interaction occurs, as characterized by the inter-scale between the bubble and the wall. In practice, it is of primary importance that the bubble undergoes a repulsive or attractive force in the wall-normal direction, which causes a lateral migration (Leal 1980; Magnaudet, Takagi & Legendre 2003; Hibiki & Ishii 2007) and determines the bubble distribution, when translating parallel to the wall. As the simplest model system, one might consider the phenomenon of

---

† Email address for correspondence: sugiyama@fel.t.u-tokyo.ac.jp

a spherical bubble rising near a vertical infinite plane wall in a creeping (Stokes) flow. However, there is no mechanism to generate the lateral migration force, as kinematic reversibility is ensured by symmetry of the boundary and by linearity in the Stokes equation (Leal 1992, chapter 4). In fact, the migration force stems from nonlinearities in the advective momentum transport (Cox & Brenner 1968; Ho & Leal 1974; Vasseur & Cox 1976, 1977; Cox & Hsu 1977; McLaughlin 1993; Cherukat & McLaughlin 1994; Becker, McKinley & Stone 1996; Magnaudet *et al.* 2003) and/or the interfacial deformability (Chaffey, Brenner & Mason 1965; Chan & Leal 1979; Shapira & Haber 1988; Uijttewaal, Nijhof & Heethaar 1993; Uijtewaal & Nijhof 1995; Magnaudet *et al.* 2003; Wang & Dimitrakopoulos 2006) to break the symmetry.

For a tank-treading vesicle translating parallel to the wall, the migration force was theoretically obtained by Olla (1997), who prescribed the vesicle shape as a strongly non-spherical ellipsoid, and the theory was experimentally validated by Callens *et al.* (2008). For a bubble or drop, the shape cannot be prescribed since it obeys the Laplace law and depends on the surrounding fluid flow. The theoretical success in solving the non-trivial problem of the deformation-induced migration of the bubble or drop was made by Magnaudet *et al.* (2003) using the Faxén mirror image technique and the Lorentz reciprocal theorem. However, Wang & Dimitrakopoulos (2006) performed a numerical study on the motion of a drop with the same viscosity as the surrounding fluid in a linear shear flow by means of a boundary element method, and pointed out that the theory considerably underestimates the migration velocity or erroneously predicts the lateral motion, despite consistent predictions of the rising velocity and the interfacial deformation. Recently, Takemura, Magnaudet & Dimitrakopoulos (2009) experimentally measured the lateral migration velocity of slightly deformed bubbles in a wall-bounded shear flow, and found a clear discrepancy between the experimental and theoretical values of the deformation-induced transverse force. Then, they computed the quasi-steady evolution of deformable bubbles moving in a wall-bounded linear shear flow at zero Reynolds number using a spectral boundary element method developed by Dimitrakopoulos (2007), and found that the measured deformation-induced lift force agrees quantitatively well with the computational prediction. Motivated by their conclusions, we revisited experimental data of the bubble migration in a quiescent liquid obtained by Takemura *et al.* (2002), and analysed the data on the conditions that the clearance between the bubble interface and the wall is comparable to or shorter than the bubble radius, which was not considered there. The results revealed that the discrepancy between the migration velocities of the experiment and the theory increased as the bubble moved closer to the wall, as detailed below.

In this paper, we focus on the bubble motion in a quiescent liquid to simplify the subject. Let us consider the migration velocity $V_{B3}(=\boldsymbol{V}_B\cdot\boldsymbol{e}_3)$ of a bubble rising near a vertical plane wall at a distance d between the bubble centroid and the wall as schematically illustrated in figure 1(a). The bubble has an equivalent radius a to that of a sphere with the same volume. Introducing an interfacial deflection $f(\theta,\phi)$ from a sphere, we write the distance from the bubble centroid to the interface as $a+f$. The experimental results used here were measured under the condition that the Reynolds number $Re=2\rho a V_{B1}/\mu$ (here $V_{B1}(=\boldsymbol{V}_B\cdot\boldsymbol{e}_1)$, ρ and μ, respectively, denote the rising velocity, the density and the dynamic viscosity of liquid) is unity or less (Takemura *et al.* 2002). The pure lateral migration velocities induced by the deformation V_{B3} were calculated from the measured values substituting the velocities induced by the inertia effects. Following a Stokes flow theory for the deformation-induced migration

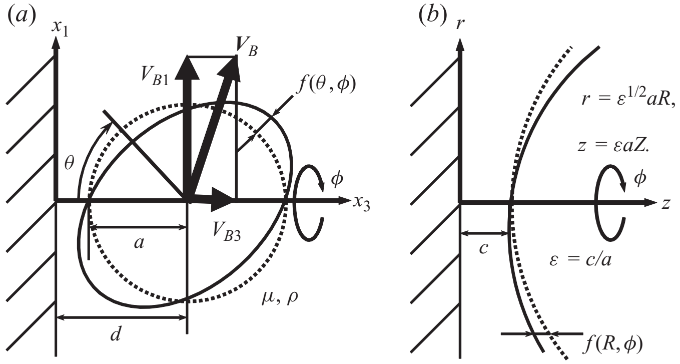

FIGURE 1. Schematic of a buoyant bubble moving near a vertical plane wall in a quiescent liquid. The solid outline shows a deformed interface with a deflection f from a spherical interface indicated by the dotted outline. (*a*) Coordinates system around the bubble. In the analysis of Magnaudet *et al.* (2003), a/d is assumed to be sufficiently smaller than unity (here, a is the bubble radius and d is the distance between the bubble centroid and the wall). (*b*) Inter-scale coordinates between the bubble surface and the wall and scaling relations suitable to lubrication theory. A clearance parameter is defined as $\varepsilon = c/a$.

(Magnaudet *et al.* 2003), we can characterize the system using two parameters, i.e. a clearance parameter $\varepsilon(= c/a)$ and a capillary number $Ca = \mu V_{B1}/\gamma$ (or a Bond number $Bo = \rho a^2 g/\gamma$ as used in Magnaudet *et al.* 2003). Here γ and g, respectively, denote the surface tension and the acceleration of gravity. Further, as long as $Ca \ll 1$, we may use Ca as a perturbation parameter, and reduce the Ca-dependent system to another, in which V_{B1}, V_{B3}/Ca and f/Ca are dependent only upon ε, under the infinitesimal deformation assumption. Figure 2 shows the migration velocity V_{B3} away from the wall normalized by $Ca V_{B1}$ as a function of $\kappa(\equiv (1+\varepsilon)^{-1})$. (It should be noticed that although κ as well as ε are measures of the distance between the wall and the bubble, hereafter κ is also used to make some equations for the wide gap case ($\kappa \ll 1$) simple.) The measured velocity is found to be much higher than the analytical solution, especially for large κ. A possible inference to be drawn from this result is that there exists an additional ingredient to generate repulsive force for a narrow bubble–wall gap, which is not covered by the theory of Magnaudet *et al.* (2003).

As the most crucial restriction involved in the mirror image technique, we can make the assumption that the bubble–wall distance is much longer than the bubble radius. However, with regard to an inertia effect on the lateral velocity of a rigid sphere, Takemura (2004) experimentally demonstrated that the mirror image approach has robust applicability in prediction beyond the wide-gap precondition. At this moment, we cannot conclude whether the discrepancy in the deformation-induced migration velocity comes from the erroneous prediction due to the miscalculation or the contradictory conditions in the boundary element computation and the experiment with the theoretical assumptions. To complement the experiment and to gain further insight into the deformation-induced migration, we investigate the migration behaviour with attention to shortness of a bubble–wall clearance $c\,(= d - a)$. As in Magnaudet *et al.* (2003), using two Stokes flow solutions for a spherical bubble translating parallel and perpendicular to the wall, we apply the Lorentz reciprocal theorem to evaluating the migration velocity. We carry out numerical simulations using a boundary-fitted grid, which can accurately implement the boundary conditions

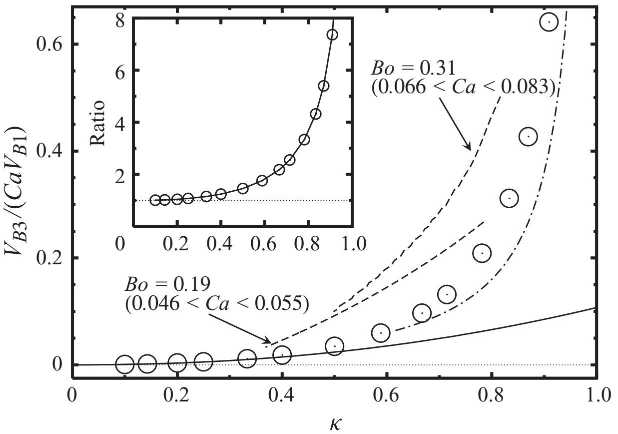

FIGURE 2. Migration velocity V_{B3} versus $\kappa(=(1+\varepsilon)^{-1})$. The solid curve indicates the analytical solution (Magnaudet *et al.* 2003) $V_{B3}/(CaV_{B1}) = 3\kappa^2(1+3\kappa/2)/\{40(1+3\kappa/4)\}$ with the assumption of the sufficiently long distance between the bubble centroid and the wall, i.e. $\varepsilon \gg 1$. The dashed curves indicate the experimental results (Takemura *et al.* 2002), the circles the results obtained by the numerical simulation and the dash-dotted curve the prediction (2.24) by means of the lubrication approach (Hodges, Jensen & Rallison 2004). The inset shows the ratio of the simulation result to the analytical solution.

and release the constraint of the sufficiently wide bubble–wall gap in the mirror image technique. In addition, comparisons with a theoretical migration velocity for $\varepsilon \ll 1$ obtained from a lubrication study of a nearly spherical drop moving near a tilted plane (Hodges *et al.* 2004), in which the secondary flow due to the change in the boundary geometry caused by the bubble deformation is responsible for the wall-normal force, are made to shed more light on the short clearance effect.

2. Numerical simulation

2.1. *General formulation*

To clarify the physical mechanism of the repulsive force, we numerically address the bubble migration. In a similar manner to Magnaudet *et al.* (2003), instead of directly solving the flow field with the deformed bubble, we employ the Lorentz reciprocal theorem to determine the lateral migration force and velocity through coupling two flow fields around a spherical bubble translating parallel and perpendicular to the wall. In the subsequent developments, the basic equations and the involved variables are non-dimensionalized using a, V_{B1} and μ. We assume that the bubble quasi-steadily rises near an infinite flat plate in a stagnant incompressible liquid, and both the Reynolds and capillary numbers are sufficiently smaller than unity. Hence, the system is described by the steady Stokes equation for solenoidal velocity vectors, i.e.

$$\nabla \cdot \boldsymbol{U} = \nabla \cdot \boldsymbol{u} = 0, \quad -\infty < x_1 < \infty, \ -\infty < x_2 < \infty, \ -1-\varepsilon \leqslant x_3 < \infty, \tag{2.1}$$

$$\nabla \cdot \boldsymbol{\Sigma} = \nabla \cdot \boldsymbol{\sigma} = 0, \quad -\infty < x_1 < \infty, \ -\infty < x_2 < \infty, \ -1-\varepsilon \leqslant x_3 < \infty, \tag{2.2}$$

where $(\boldsymbol{U}, \boldsymbol{\Sigma})$ and $(\boldsymbol{u}, \boldsymbol{\sigma})$ are the velocity and stress fields for the bubble translating, respectively, parallel and perpendicular at a speed of unity to the wall. The Ca dependence of the interfacial deflection is given by $f(\theta, \phi; Ca) = Ca\, f^{(Ca)}(\theta, \phi)$. The bubble deformation obeys the Laplace law for the infinitesimal deflection $|f| \ll 1$ with

$Ca \ll 1$,

$$\left(\nabla_s^2 + 2\right) f^{(Ca)} = -\boldsymbol{n}\cdot\boldsymbol{\Sigma}\cdot\boldsymbol{n} + 3x_1\langle x_1\boldsymbol{n}\cdot\boldsymbol{\Sigma}\cdot\boldsymbol{n}\rangle_{S_B}, \quad \text{at} \quad \sqrt{x_1^2+x_2^2+x_3^2} = 1, \tag{2.3}$$

where $\boldsymbol{n}$ represents the normal unit vector pointing outwards from the liquid, $\nabla_s(=\nabla - \boldsymbol{n}(\boldsymbol{n}\cdot\nabla))$ is the nabla operator along the tangential directions on the bubble surface, $\langle\ldots\rangle_{S_B}$ is the area average taken over the bubble surface and x_1 is the coordinate in the upward direction from the origin at the bubble centroid. Kinematic and free-slip conditions are imposed on the bubble surface, i.e.

$$\left.\begin{aligned} \boldsymbol{n}\cdot\boldsymbol{U} &= 0, \\ (\boldsymbol{n}\cdot\boldsymbol{\Sigma})\times\boldsymbol{n} &= 0, \\ \boldsymbol{n}\cdot\boldsymbol{u} &= 0, \\ (\boldsymbol{n}\cdot\boldsymbol{\sigma})\times\boldsymbol{n} &= 0, \end{aligned}\right\} \quad \text{at} \quad \sqrt{x_1^2+x_2^2+x_3^2} = 1, \tag{2.4}$$

where we take the reference frames viewed from the bubble. On the plane wall, we impose the no-slip condition

$$\left.\begin{aligned} \boldsymbol{U} &= -\boldsymbol{e}_1, \\ \boldsymbol{u} &= \boldsymbol{e}_3, \end{aligned}\right\} \quad \text{at} \quad x_3 = -1-\varepsilon. \tag{2.5}$$

Sufficiently far from the bubble, the velocity vectors approach the uniform velocities

$$\left.\begin{aligned} \boldsymbol{U} &\to -\boldsymbol{e}_1, \\ \boldsymbol{u} &\to \boldsymbol{e}_3, \end{aligned}\right\} \quad \text{as} \quad \sqrt{x_1^2+x_2^2+x_3^2} \to \infty. \tag{2.6}$$

Thanks to the reciprocal theorem (Leal 1980; Magnaudet *et al.* 2003, equation (35)), the deformation-induced lateral force $F_M = Ca F_M^{(Ca)}$ to cancel the migration velocity and to maintain the wall-parallel motion is expressed as

$$F_M^{(Ca)} = \oint_{S_B} \mathrm{d}^2\boldsymbol{x}\ \mathscr{L}\left(f^{(Ca)}\right), \tag{2.7}$$

where S_B denotes the bubble surface, and the operator $\mathscr{L}$ is given by

$$\begin{aligned} \mathscr{L} = \boldsymbol{n}\cdot\boldsymbol{\sigma}\cdot\boldsymbol{n}\left(\frac{\partial\boldsymbol{U}}{\partial n}\cdot\boldsymbol{n} - \boldsymbol{U}\cdot\nabla_s\right) - \boldsymbol{u}\cdot\left(\frac{\partial\boldsymbol{\Sigma}}{\partial n}\cdot\boldsymbol{n} - \boldsymbol{\Sigma}\cdot\nabla_s\right) \\ - \left\{\boldsymbol{n}\cdot\boldsymbol{\Sigma}\cdot\boldsymbol{n} - 3x_1\langle x_1\boldsymbol{n}\cdot\boldsymbol{\Sigma}\cdot\boldsymbol{n}\rangle_{S_B}\right\}\boldsymbol{u}\cdot\nabla_s. \end{aligned} \tag{2.8}$$

The migration velocity $V_{B3} = Ca V_{B3}^{(Ca)}$ is expressed as

$$\frac{V_{B3}^{(Ca)}}{V_{B1}} = \frac{F_M^{(Ca)}}{F_{DC}}, \tag{2.9}$$

where

$$F_{DC} = \oint_{S_B} \mathrm{d}^2\boldsymbol{x}\ \boldsymbol{e}_3\cdot\boldsymbol{\sigma}\cdot\boldsymbol{n} \tag{2.10}$$

denotes the drag force acting on the bubble translating perpendicular to the plane wall.

2.2. *Simulation method*

The basic equations are numerically solved by the second-order finite-difference method discretized on a bipolar coordinates (ξ, η) grid, which is boundary-fitted on both the bubble surface and the plane wall (see figure 9*a* in Appendix A).

We take care of the mass and momentum conservations in a discretized form. For technical detail on the discretization, see Appendix A. The number of grid points is $N_\xi \times N_\eta = 200 \times 200$, and the grid is non-uniform and refined near the wall and the bubble surface. The computational procedure is based on a simplified-marker-and-cell method (Amsden & Harlow 1970) with a first-order Eulerian implicit time marching scheme. Such an unsteady scheme enables us to check whether the computation converges to the fully developed state through temporal changes in the budgets of the momentum and kinetic-energy transports. To avoid a problem associated with singularities in the discretization near the axis, we follow a method proposed by Fukagata & Kasagi (2002).

For each run, we confirm that drag forces, numerically evaluated on the bubble surface, for both the perpendicular and parallel motions are in good agreement with the respective kinetic-energy dissipation rates, numerically integrated over the entire computational domain, normalized by the translational velocities with an error of less than 0.040 %. Such an agreement between the surface and bulk quantities indicates that the computation is well converged and reaches to the steady state in view of the momentum and kinetic-energy budgets. Further, the drag force for the perpendicular motion shows quantitative agreement with the infinite series solution of Bart (1968) with an error of less than 0.043 %. The drag force for the parallel motion approaches the wide-gap solution of Magnaudet *et al.* (2003) with increasing ε. To make sure of numerical stability and accuracy, we set the clearance parameter in a range of $10^{-3} \leqslant \varepsilon \leqslant 9$. We performed the convergence tests by varying the size R_{max} of the computational domain, the number N_ξ of nodes in the gap between the bubble and the wall, and the number N_η of nodes describing the bubble surface. We confirmed that the relative errors in the migration velocity V_{B3} and the drag forces for the perpendicular and parallel bubble motions, to those obtained on the base meshes $N_\xi \times N_\eta = 200 \times 200$ for various ε, decrease when increasing the size R_{max} and the resolutions N_ξ and N_η. From the convergence behaviour, we deduce the migration velocities V_{B3} with errors of much less than 1 %, using the present base meshes, which are accurate enough for the subsequent discussion.

2.3. *Migration velocity*

As shown in the inset of figure 2, the ratio of the simulation to the analytical migration velocity becomes close to unity as $\kappa (= (1+\varepsilon)^{-1})$ approaches zero, indicating the simulation result is consistent with the analytical solution (Magnaudet *et al.* 2003) for small $\kappa (< \sim 0.3)$. Such a consistency between the different approaches may refute the erroneous prediction of the migration velocity in Magnaudet *et al.* (2003), of which the possibility was pointed out by Wang & Dimitrakopoulos (2006). By contrast, the simulated migration velocity for the bubble closer to the wall with the clearance shorter than the bubble radius (i.e. for $\kappa > \sim 0.5$ presumably beyond the theoretical precondition $\kappa \ll 1$) is considerably higher than the analytical solution. Although the simulation result reveals a lower velocity than the experimental one, the tendency to a higher velocity than the theoretical one for the narrow gap is qualitatively similar to that in the experiment. Thus, the present simulation also indicates the presence of the additional narrow-gap repulsive force.

For an undeformed spherical bubble at small but non-zero Reynolds numbers $0 < Re \ll 1$, using the solutions to (2.1)–(2.6), we can also evaluate the inertia effect on the migration velocity $V_{B3} = Re\ V_{B3}^{(Re)}$ from

$$F_M^{(Re)} = \frac{1}{2} \int_{\mathscr{V}} \mathrm{d}^3 \boldsymbol{x}\ (\boldsymbol{e}_3 - \boldsymbol{u}) \cdot \{(\boldsymbol{U} \cdot \nabla) \boldsymbol{U}\}, \tag{2.11}$$

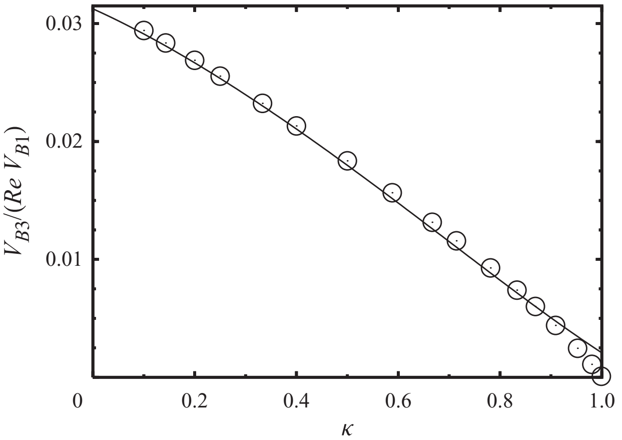

FIGURE 3. Inertia-driven migration velocity V_{B3} versus $\kappa(=(1+\varepsilon)^{-1})$ for spherical bubble at $0<Re\ll 1$. The solid curve indicates the analytical solution (Magnaudet *et al.* 2003) $V_{B3}/(ReV_{B1})=((1+\kappa/8-0.516\kappa^2)/32)(1-(3/4)\kappa-(9/64)\kappa^4)$ under the assumption of $(O(Re)<\kappa\ll 1)$ as in figure 2. The circles indicate the results obtained by the numerical simulation.

$$\frac{V_{B3}^{(Re)}}{V_{B1}}=\frac{F_M^{(Re)}}{F_{DC}}, \tag{2.12}$$

where $\mathscr{V}$ stands for the entire volume of liquid around the bubble. The force expression (2.11) is theoretically justified for the case that the wall is placed within a Stokes expansion region, i.e. $O(Re)<\kappa$ (Vasseur & Cox 1976). Figure 3 shows the inertia-driven migration velocity as a function of κ. The simulated profile is globally consistent with the analytical solution (Magnaudet *et al.* 2003) even for the narrow gap $\kappa\sim 1$, as opposed to the profile of the deformation-induced migration velocity in figure 2. It should be noticed that (2.7) of the deformation-induced lateral force is written in a surface integral form, while the inertia-driven force (2.11) in a volume integral form. The overall agreement in the inertia-driven migration velocity indicates that capturing the bulk velocity distributions is important for predicting the migration velocity and can be robustly attained by the mirror image technique over the wide range of κ. The wide range of agreement with the theories (Vasseur & Cox 1976; Magnaudet *et al.* 2003) was also experimentally demonstrated for the sedimenting rigid particle in a range of $0.1<Re<1$ by Takemura (2004) as long as the wall is placed in the Stokes expansion region. Contrastingly, as shown in figure 2, the larger discrepancy between the deformation-induced migration velocities of the simulation and the theory with increasing κ indicates that the migration velocity is sensitive to the local effect leading to the additional narrow-gap repulsive force, which may not be covered by the mirror image technique.

2.4. *Interfacial deformation*

To demonstrate the narrow-gap effect, we investigate the bubble deformation. We here examine the scaled interfacial deflection $\hat{f}^{(Ca)}(\theta)=f(\theta,\phi)/(Ca\ \cos\phi)$. In the experiment, we estimated $f(\theta,\phi)$ taking a circumference of the bubble on the plane $x_2=0$. Figure 4 shows the angular profile of the deflection $-\hat{f}^{(Ca)}$ for various $\kappa(=(1+\varepsilon)^{-1})$. As shown in figure 4(*a*) for the relatively wide gap $\varepsilon=0.67$, the analytical solution for $\kappa\ll 1$ (Magnaudet *et al.* 2003) is consistent with the measured and simulated deflections. Note that the agreement between the theoretical and

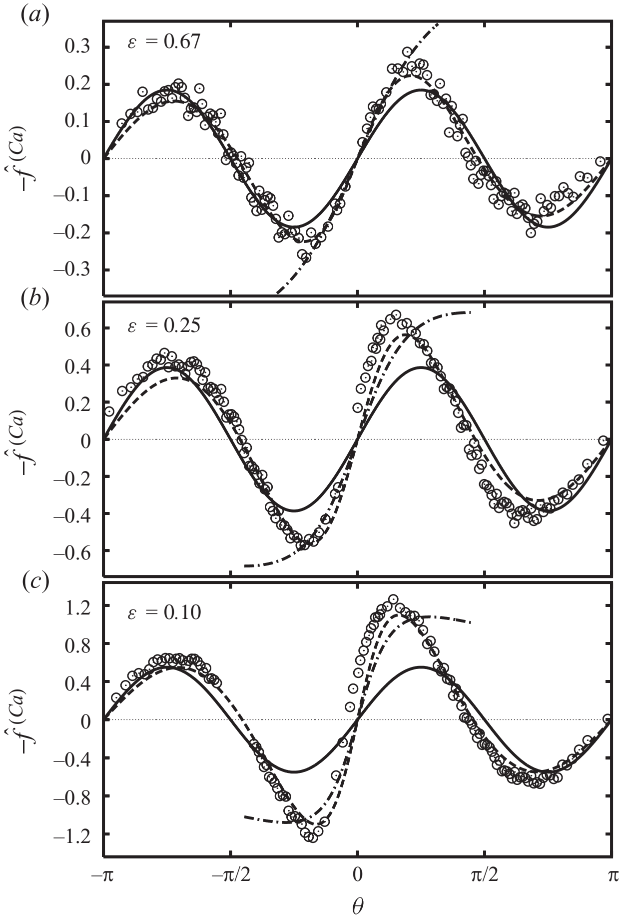

FIGURE 4. Angular profile of the deflection. The solid curves indicate the analytical solution (Magnaudet *et al.* 2003) $-\hat{f}^{(Ca)} = (3/4)\kappa^2 \{1+(3/8)\kappa\ (1+(3/8)\kappa+(73/64)\ \kappa^2)\} \sin\theta\cos\theta$ with the assumption of the sufficiently long distance between the bubble centroid and the wall, i.e. $\kappa(=(1+\varepsilon)^{-1}) \ll 1$. The circles indicate the experimental results (Takemura *et al.* 2002), the dashed curves the results obtained by the numerical simulation and the dash-dotted curves the prediction (B 11) $(-\hat{f}^{(Ca)} = (3/5\theta)\log(1+\theta^2/2\varepsilon))$ by the lubrication approach (Hodges *et al.* 2004). The results at $\varepsilon = 0.67$, $\varepsilon = 0.25$ and $\varepsilon = 0.10$ are shown in (*a*), (*b*) and (*c*), respectively, and the corresponding capillary numbers in the experiment are $Ca = 0.080$, $Ca = 0.068$ and $Ca = 0.056$, respectively.

simulated deflections is confirmed to be better in the wider separation. For the narrower gap ($\varepsilon = 0.10$, 0.25), by contrast, the analytical solution of the deflection magnitude is smaller than the measured one, especially in the wall neighbourhood ($\theta \sim 0$), which may be related to the considerable underestimation of the migration velocity as shown in figure 2. In contrast, the present simulation quantitatively captures the local near-wall profile of the measured deflection as well as the global magnitude.

To quantify the local effect of such a large discrepancy in $\hat{f}^{(Ca)}$ on the migration velocity, we describe the deflection in an expansion form,

$$\hat{f}^{(Ca)}(\theta) = \sum_{n=2}^{\infty} \hat{f}_n^{(Ca)} P_n^1(\cos\theta), \tag{2.13}$$

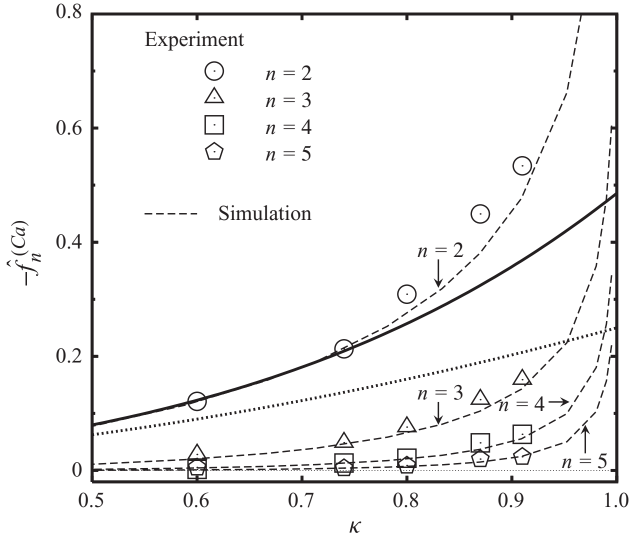

FIGURE 5. Modal deflection, $\hat{f}_n^{(Ca)}$, which is expanded in associated Legendre polynomials P_n^1, versus $\kappa(=(1+\varepsilon)^{-1})$. The dotted curve indicates the leading term of the analytical solution (Magnaudet *et al.* 2003) $\hat{f}_n^{(Ca)}=\kappa^2/4$ and the solid curve indicates the analytical solution with the higher-order contributions $\hat{f}_n^{(Ca)}=\kappa^2/4\ \{1+(3/8)\kappa\ (1+(3/8)\kappa+(73/64)\kappa^2)\}$. The symbols indicate the experimental results (Takemura *et al.* 2002) and the dashed curves indicate the results obtained by the numerical simulation.

where P_n^1 represents the associated Legendre polynomial. Figure 5 shows the modal deflections $\hat{f}_n^{(Ca)}$ for $2\leqslant n\leqslant 5$ as a function of κ. The simulation results are consistent with the measured deflections for all the shown modes. In predicting the bubble migration, the wide-gap theory (Magnaudet *et al.* 2003) assumes that the mirror image primarily induces the deformation of the mode $n=2$. The leading order of the $n=2$ deflection is $\hat{f}_2^{(Ca)}=\kappa^2/4$ in the limit of $\kappa\rightarrow 0$. Considering the higher-order effect with respect to κ, Magnaudet *et al.* (2003) derived $\hat{f}_n^{(Ca)}=\kappa^2/4\ \{1+(3/8)\kappa\ (1+(3/8)\kappa+(73/64)\kappa^2)\}$. For $\kappa<\sim 0.7$, such a higher-order κ correction is responsible for the enhancement of the $n=2$ deflection from the leading-order one, as seen in the better agreement with the measured and simulated deflections. However, the correction is not sufficient for the narrower gap $\kappa>\sim 0.7$, and thus the theoretical underestimation of the $n=2$ deflection becomes more serious with κ. Further, the theory does not cover the considerable increase in the higher-order $n\geqslant 3$ deflections with κ, as demonstrated by both the measurement and the simulation.

The modal deflection $\hat{f}_n^{(Ca)}$ is linked to the migration velocity and force as decomposed into

$$V_{B3}^{(Ca)}=\sum_{n=2}^{\infty}V_{B3,n}^{(Ca)},\quad F_M^{(Ca)}=\sum_{n=2}^{\infty}F_{M,n}^{(Ca)}, \tag{2.14}$$

which are

$$\frac{V_{B3,n}^{(Ca)}}{V_{B1}}=\frac{F_{M,n}^{(Ca)}}{F_{DC}}, \tag{2.15}$$

$$F_{M,n}^{(Ca)}=\oint_{S_B}\mathrm{d}^2\boldsymbol{x}\ \mathscr{L}\big(\hat{f}_n^{(Ca)}P_n^1(\cos\theta)\cos\phi\big). \tag{2.16}$$

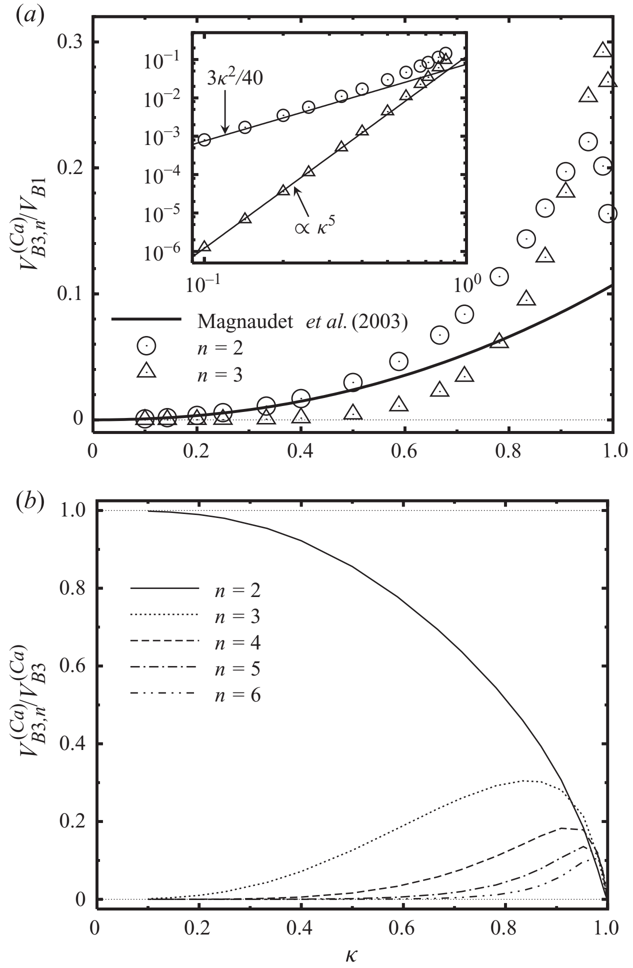

FIGURE 6. Contribution of the modal deflection to the migration velocity $V^{(Ca)}_{B3,n}$, which is expanded in associated Legendre polynomials P^1_n. (a) The linear–linear plot of the velocity of the modes $n = 2$ and $n = 3$ versus $\kappa(= (1 + \varepsilon)^{-1})$. The solid line indicates the analytical solution (Magnaudet *et al.* 2003) $V^{(Ca)}_{B3,2}/V_{B1} = 3\kappa^2(1 + 3\kappa/2)/\{40(1 + 3\kappa/4)\}$. The symbols indicate the results obtained by the numerical simulation. The inset shows the same plot in a log–log scale. (b) The simulation results of the modal contribution normalized by the total velocity.

Figure 6(a) shows the contribution of the modal deflection to the migration velocity for the modes $n = 2$ and $n = 3$. For small κ, the simulation result is consistent with the analytical solution (Magnaudet *et al.* 2003), which considers only the $n = 2$ deformation to cause the bubble migration. The inset shows that for small κ, the contribution of the mode $n = 2$ is proportional to κ^2, while that of the mode $n = 3$ to κ^5, whose exponent is not trivially proved, but may be predictable, extending the regular perturbation to the higher order. The difference in the exponent ensures that the relative contribution of the mode $n = 3$ to $n = 2$ becomes more significant with κ. It should be noticed that although we confirmed that the migration force contribution $F^{(Ca)}_{M,2}$ of the mode $n = 2$ increases as $\kappa \to 1$ (i.e. $\varepsilon \to 0$), the velocity contribution $V^{(Ca)}_{B3,2}$ reduces as shown in figure 6(a). It is because the slope of the $n = 2$ migration force, $-\mathrm{d}\log F^{(Ca)}_{M,2}/\mathrm{d}\log\varepsilon$, in a logarithmic plot is more gentle than that of the drag force, $-\mathrm{d}\log F_{DC}/\mathrm{d}\log\varepsilon \to 1$, in the denominator of (2.15) as $\varepsilon \to 0$. Figure 6(*b*) shows the modal contribution $V_{B3,n}^{(Ca)}$ compared with the migration velocity $V_{B3}^{(Ca)}$. The contribution of the mode $n=2$ monotonically decreases with κ. The contribution of the mode $n=3$ increases with κ in the range of $\kappa < \sim 0.8$, while it decreases for greater κ. This is because the higher modal contributions for $n \geqslant 4$ can no longer be disregarded. Moreover, the fact that all the modal contributions shown decay as $\kappa \to 1$ indicates that the further higher-order contributions become considerable, and the regular perturbation approach with respect to κ is no longer effective.

2.5. *Comparison with small deformation theory in the lubrication limit*

Figures 4, 5 and 6 imply that for small ε, the bubble deformation is preferentially enhanced within the narrow bubble–wall gap, and then its squeezing effect promotes the bubble migration. To shed more light on the role of the hydrodynamics in the gap, comparisons with a small deformation theory in the lubrication limit will be made. It should be noticed that Hodges *et al.* (2004) have performed a lubrication study for a nearly spherical drop near a tilted plane in so-called 'slipping' regime, and derived the deformation-induced normal force. One can also access a relevant physical picture in theoretical studies on the lift force on an elastic body induced by its deformation (Sekimoto & Leibler 1993; Skotheim & Mahadevan 2004, 2005; Urzay, Smith & Glover 2007). Following the spirit of the lubrication theory, we evaluate the migration velocity in the limit of $\varepsilon \to 0$.

The basic equations for the lubrication analysis and the solutions are shown in Appendix B. For comparison with the simulation results, the preconditions and the perturbed quantities are detailed here. We prescribe the wall-parallel velocity V_{B1}, and employ the standard lubrication assumption, i.e. $\varepsilon \ll 1$. We also assume a small capillary number $Ca \ll 1$. As implied in (2.21), the deflection is $O(Ca\varepsilon^{-1/2}a)$, which has to be sufficiently smaller than the gap εa if the tilt angle of the near-wall interface from the plane wall is assumed to be small. Here we adopt an additional constraint $\delta \equiv \varepsilon^{-3/2}Ca \ll 1$. For inner coordinates (R, Z, ϕ) (here $\varepsilon^{1/2}R = r$ and $\varepsilon^{-1}Z = z$ as illustrated in figure 1*b*; see e.g. Goldman, Cox & Brenner 1967; O'Neill & Stewartson 1967), a parabolic profile $Z = H(R) \equiv 1 + R^2/2$ represents the interface within the inner region $r \sim \varepsilon^{1/2}$, if the deformation is absent. Using ε, we write the velocity vector, the pressure and the deflection $f^{(Ca)}$ of the interface in an expansion form with respect to δ:

$$\begin{aligned} u_r(r,\phi,z) = {} & \hat{U}_r^{(0)}(R,Z)\cos\phi + \delta\hat{U}_r^{(f)}(R,Z) + \varepsilon\hat{U}_r^{(1)}(R,Z)\cos\phi \\ & + \delta\hat{U}_r^{(f,2)}(R,Z)\cos 2\phi + O(\delta^2) + O(\varepsilon\delta) + \cdots, \end{aligned} \tag{2.17}$$

$$\begin{aligned} u_\phi(r,\phi,z) = {} & \hat{U}_\phi^{(0)}(R,Z)\sin\phi + \varepsilon\hat{U}_\phi^{(1)}(R,Z)\sin\phi \\ & + \delta\hat{U}_\phi^{(f,2)}(R,Z)\sin 2\phi + O(\delta^2) + O(\varepsilon\delta) + \cdots, \end{aligned} \tag{2.18}$$

$$\begin{aligned} u_z(r,\phi,z) = {} & \varepsilon^{1/2}\big(\hat{U}_z^{(0)}(R,Z)\cos\phi + \delta\hat{U}_z^{(f)}(R,Z) + \varepsilon\hat{U}_z^{(1)}(R,Z)\cos\phi \\ & + \delta\hat{U}_z^{(f,2)}(R,Z)\cos 2\phi + O(\delta^2) + O(\varepsilon\delta) + \cdots\big), \end{aligned} \tag{2.19}$$

$$\begin{aligned} p(r,\phi,z) = {} & \varepsilon^{-3/2}\big(\hat{P}^{(0)}(R)\cos\phi + \delta\hat{P}^{(f)}(R) + \varepsilon\hat{P}^{(1)}(R,Z)\cos\phi \\ & + \delta\hat{P}^{(f,2)}(R,Z)\cos 2\phi + O(\delta^2) + O(\varepsilon\delta) + \cdots\big), \end{aligned} \tag{2.20}$$

$$f^{(Ca)}(r,\phi) = \varepsilon^{-1/2}\big(\hat{F}(R)\cos\phi + O(\delta) + O(\varepsilon)\big), \tag{2.21}$$

whose scaling relations are suitable for all equations in Appendix B. It should be noted that the terms with the superscript (0), (1) or $(f, 2)$ in (2.17)–(2.20) are proportional to $\cos\phi$, $\sin\phi$, $\cos 2\phi$ or $\sin 2\phi$, and thus provide no wall-normal force. Here we make it clear that the physical domain of validity of the condition $\delta \ll 1$ when the rising velocity V_{B1}, which is needed to evaluate $Ca(=\mu V_{B1}/\gamma)$, is unknown. Following the analysis by O'Neill & Stewartson (1967), we write the drag force F_D acting on the spherical bubble translating parallel to the wall in a form $\boldsymbol{F_D} = 6\pi\mu a V_{B1}(A\log\varepsilon + B)$, where A and B are independent of ε. Considering the free-slip boundary condition on the bubble surface, we can analytically find $A = -1/5$. From our numerical data, we approximately estimate $B = 0.6$. Hence, from the force balance $F_D = 4\pi\rho a^3 g/3$, for $\varepsilon \ll 1$, we evaluate the rising velocity

$$V_{B1} = \frac{1}{(-\log\varepsilon + 3)}\frac{10\rho a^2 g}{9\mu}, \tag{2.22}$$

and obtain the following relation for the bubble radius a to satisfy the condition $\delta \ll 1$:

$$a \ll \sqrt{\frac{9\gamma}{10\rho g}}\,\varepsilon^{3/4}(-\log\varepsilon + 3)^{1/2}. \tag{2.23}$$

To assure us of the appearance of the lubrication effect, figure 7 shows the profiles of the pressure $\hat{P}^{(0)}(= 3R/(5H^2))$ and deflection $-\hat{F}(= 3\log H/(5R))$ in the lubrication limit (see (B 10) and (B 11), respectively), which are compared with the simulation results of the scaled interfacial pressure $\varepsilon^{3/2}P/\cos\phi$ and the scaled deflection $\varepsilon^{1/2}\hat{f}^{(Ca)}$ near the wall as a function of $\varepsilon^{-1/2}\theta$. For sufficiently small ε, the simulation data of the scaled pressure collapse onto the curve (B 10) as shown in figure 7(*a*). Therefore, the scaled deflection profile approaches the lubrication solution (B 11) when decreasing the bubble–wall gap, as shown in figure 7(*b*). As plotted as the dashed-dotted curve in figure 4, the deflection based on (2.21) and (B 11) is consistent with the measured and simulated deflections in the wall neighbour ($\theta \sim 0$). Hence, the discrepancy between the deflections of the narrow-gap experiment and the wide-gap theory (Magnaudet *et al.* 2003) is attributable to the lubrication effect.

From Bart (1968), the drag force acting on the bubble translating perpendicular to the plane wall is $F_{DC} \to 3\pi\mu/(2\varepsilon)$ as $\varepsilon \to 0$. Substituting this relation and (B 20) (i.e. F_M in the lubrication limit) into (2.9), we obtain the asymptotic solution of the migration velocity

$$\frac{V_{B3}}{V_{B1}} = \frac{F_M}{F_{DC}} \to \frac{Ca}{25}\varepsilon^{-1} \quad \text{as} \quad \varepsilon \to 0. \tag{2.24}$$

To make comparisons with the asymptotic solutions, figures 2 and 8 show the scaled migration velocity as functions of the inverse distance $\kappa(=(1+\varepsilon)^{-1})$ and the clearance parameter ε, respectively. The inset of figure 8 shows the scaled force (B 20). The simulation results are consistent with two asymptotic behaviours based on the lubrication theory for $\varepsilon \ll 1$ as well as the mirror image technique for $\varepsilon \gg 1$ (i.e. $\kappa \ll 1$). As seen from figure 8, the theories provide the different exponents of the migration velocity scaling with respect to ε, namely, $V_{B3}/V_{B1} \propto Ca\ \varepsilon^{-2}$ for $\varepsilon \gg 1$ and $V_{B3}/V_{B1} \propto Ca\ \varepsilon^{-1}$ for $\varepsilon \ll 1$.

The puzzling finding in Takemura *et al.* (2009) that the theory of Magnaudet *et al.* (2003) accurately predicts the deformation but fails to predict quantitatively the deformation-induced migration velocity is explained by the fact that the ratio of the simulation result of V_{B3} to the theoretical prediction is more sensitively dependent upon ε than that of $\hat{f}_2^{(Ca)}$ when the lubrication effect becomes relevant. For instance, for $\varepsilon = 0.4$, $\varepsilon = 0.2$ and $\varepsilon = 0.1$, the simulation-to-theory ratios of $\hat{f}_2^{(Ca)}$ are, respectively,

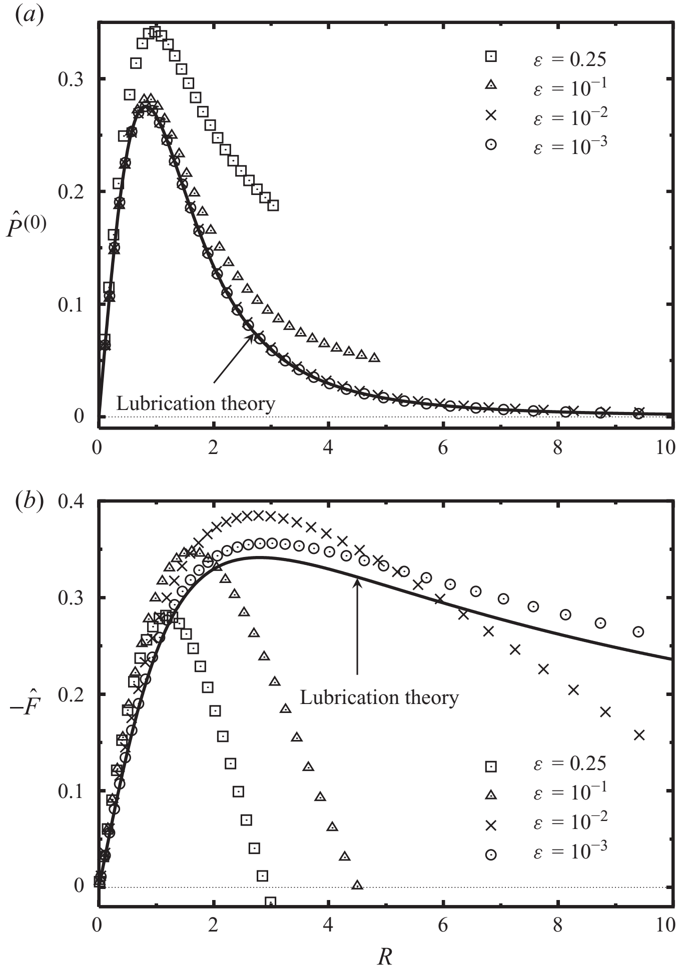

FIGURE 7. Profiles of the pressure (*a*) and the deflection (*b*) in the inner expansion scalings of the lubrication theory. The solid curves indicate the predictions (B 10) and (B 11) by the lubrication approach (Hodges *et al.* 2004). The symbols indicate the results obtained by the numerical simulation. For the plot, the simulation data of the interfacial pressure P and deflection $\hat{f}^{(Ca)}$ for the bubble translating parallel to the wall are scaled as $\hat{P}^{(0)} = \varepsilon^{-3/2}P/\cos\phi$ and $\hat{F} = \varepsilon^{-1/2}\hat{f}^{(Ca)}$, and the angular coordinate as $R = \varepsilon^{-1/2}\theta$.

1.004, 1.1 and 1.3 (figure 5), while those of V_{B3} are, respectively, 2.5, 4.3 and 7.3 (figure 2). The lubrication effect is likely to compensate for the large discrepancy between the migration velocities of the experiment and the wide-gap theory revealed in Takemura *et al.* (2009). However, although the quantitative agreement between the interfacial deflections of the experiment and the simulation is shown in figures 4 and 5, the migration velocity in the experiment is still considerably higher than the simulated one. The cause is not clear at the moment, and further joint research combining theory, numerics and experiment is needed to resolve this discrepancy.

3. Conclusion

We numerically and theoretically investigated deformation-induced lateral migration of a bubble slowly rising near a vertical plane wall in a stagnant liquid.

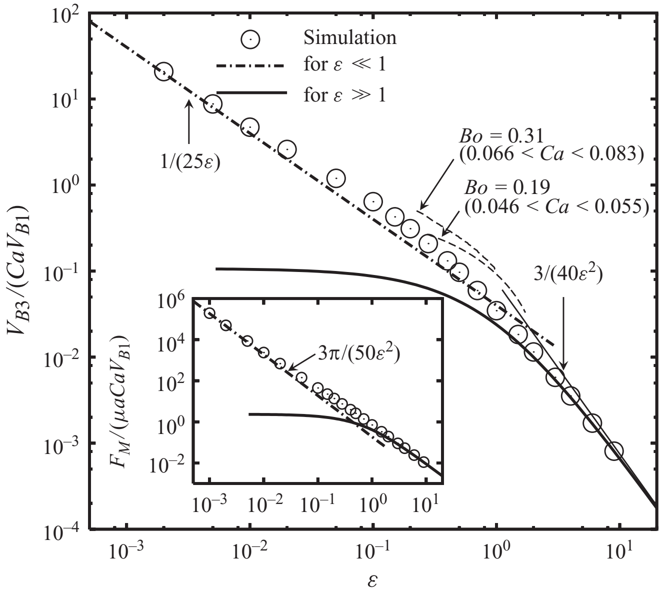

FIGURE 8. The lateral migration velocity versus the clearance parameter ε. The circles indicate the results obtained by the numerical simulation. The solid and dash-dotted curves correspond to the analytical solution $V_{B3} = 3CaV_{B1}\kappa^2\ (1 + 3\kappa/2)/\{40(1 + 3\kappa/4)\}$ (Magnaudet *et al.* 2003) and $V_{B3} = CaV_{B1}\varepsilon^{-1}/25$, respectively, derived by means of the lubrication approach (Hodges *et al.* 2004). The dashed curves indicate the experimental results (Takemura *et al.* 2002). The inset shows the lateral force (B 20).

We focused on a situation with a short clearance c between the bubble interface and the wall. We demonstrated that the wide-gap theory (Magnaudet *et al.* 2003), which considers the $n = 2$ deformation mode, describes the deformation-induced lift force as long as the bubble–wall gap is sufficiently wide ($a/(a + c) \ll 1$, here a is the bubble radius). For the narrow-gap case with the clearance parameter $\varepsilon(= c/a)$ smaller than unity, we found that the higher-order $n \geqslant 3$ deformation modes crucially enhance the migration velocity, and the lubrication effect (Hodges *et al.* 2004) appears to induce the migration velocity, which scales asymptotically like $V_{B3} \to Ca\ \varepsilon^{-1} V_{B1}/25$ as $\varepsilon \to 0$. This contrasts with the case of the inertia-driven migration, to which the wide-gap theory demonstrated a robust applicability in prediction over a wide range of ε.

The present simulation consistently served as bridge between the wide- and narrow-gap theories (see figure 8) as long as the bubble deformation is assumed to be infinitesimal. However, in spite of the qualitative success of the simulation in revealing the narrow-gap repulsive force, the deformation-induced migration velocity in the experiment is considerably higher by a factor of about 3 than the simulated one, as shown in figure 2. The experiment may inevitably involve unknown factors such as unsteadiness, imperfection from the infinite plate-fluid system and measurement uncertainty, which cannot be captured by the simulation. Nevertheless, we have not expected such a large discrepancy because (i) the quantitative agreement between the interfacial deflections of the experiment and the simulation has been confirmed in figures 4 and 5, (ii) the inertia-driven migration velocity of a rigid sphere is consistent with the available theories (Vasseur & Cox 1976; Magnaudet *et al.* 2003) has been obtained by Takemura (2004) using the same experimental set-up, and (iii) considerable uncertainty seems not to be introduced into such a simple system, as illustrated in figure 1. Further joint research combining theory, numerics and experiment is needed to resolve this problem. As a possible factor causing the inconsistency, we note the difference between the bubble deformation levels of the experiment and the present analysis. As stated in § 2.5, the infinitesimal deformation assumption in the lubrication limit is justified only for the case that $\delta(=\varepsilon^{-3/2}Ca) \ll 1$. Beyond this limitation, unexplored hydrodynamic ingredients possibly become important on the bubble migration. For the experimental data shown in figures 2 and 8, the maximum value of δ is 0.74, which is less than but comparable to unity. Therefore, the bubble deformation is finite rather than infinitesimal, and is likely to induce the higher-order force, which is possibly comparable to or stronger than the leading migration force evaluated with the infinitesimal deformation theories. From the theoretical viewpoint, a tiny bubble experiment, which results in a tiny capillary number and thus a tiny deformation, is favourable for comparative study. However, such an experiment has often resulted in an undetectable low migration velocity and made accurate measurement difficult. To overcome such a dilemma, the highly accurate boundary element computations (e.g. Wang & Dimitrakopoulos 2006; Dimitrakopoulos 2007) for various deformation levels would be helpful to complement the infinitesimal deformation theories.

We thank Shu Takagi for fruitful discussion.

Appendix A. Finite-difference descriptions of the basic equation set in bipolar coordinates

We describe the basic equation set in bipolar coordinates (see e.g. O'Neill 1964; Happel & Brenner 1973, Appendix A-19) as illustrated in figure 9(*a*). The coordinates (r, z) in figure 1(*b*) are

$$r = \frac{k \sin\eta}{\mathscr{D}}, \quad z = \frac{k \sinh\xi}{\mathscr{D}}, \tag{A 1}$$

where $\mathscr{D} = \cosh\xi - \cos\eta$ and $k = \sqrt{\varepsilon(\varepsilon + 2)}$. The bubble surface is located at $\xi = \alpha \equiv \log(1 + \varepsilon + k)$ as shown in figure 9(*a*). The gradient of a scalar function q is written as

$$\nabla q = \frac{\boldsymbol{e}_\xi}{h_\xi}\frac{\partial q}{\partial \xi} + \frac{\boldsymbol{e}_\eta}{h_\eta}\frac{\partial q}{\partial \eta} + \frac{\boldsymbol{e}_\phi}{h_\phi}\frac{\partial q}{\partial \phi}, \tag{A 2}$$

where $\boldsymbol{e}$ represents a unit vector, and its subscript the corresponding component; h denotes the scale factor, defined by, e.g. $h_\xi = \{(\partial x_1/\partial_\xi)^2 + (\partial x_2/\partial_\xi)^2 + (\partial x_3/\partial_\xi)^2\}^{1/2}$ (see e.g. Batchelor 1967, Appendix B). Each component is explicitly given by

$$h_\xi = h_\eta = \frac{k}{\mathscr{D}}, \quad h_\phi = r. \tag{A 3}$$

The vector and pressure field $(\boldsymbol{U}, P)$ for the bubble translating parallel to the wall is written in the form (e.g. Sugiyama & Sbragaglia 2008)

$$\boldsymbol{U} = \{(\boldsymbol{e}_\xi \hat{U}_\xi + \boldsymbol{e}_\eta \hat{U}_\eta)\cos\phi + \boldsymbol{e}_\phi \hat{U}_\phi \sin\phi - \boldsymbol{e}_1\}, \quad P = \hat{P}\cos\phi, \tag{A 4}$$

for which the Fourier expansion reduces the three-dimensional problem to a two-dimensional one. The vector and pressure field $(\boldsymbol{u}, p)$ for the bubble translating perpendicular to the wall is

$$\boldsymbol{u} = \boldsymbol{e}_\xi \hat{u}_\xi + \boldsymbol{e}_\eta \hat{u}_\eta + \boldsymbol{e}_3, \quad p = \hat{p}. \tag{A 5}$$

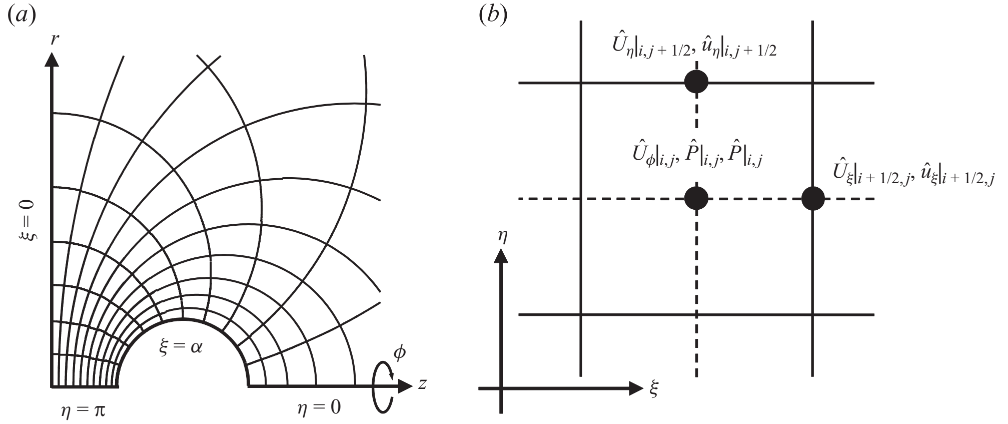

FIGURE 9. Computational grid. (*a*) The bipolar coordinates: $\xi = 0$ and $\xi = \alpha$ represent the plane wall and the bubble surface, respectively. (*b*) Definition points of the velocity components and the pressures on the staggered grid in a computational space.

It should be noticed that, as opposed to the reference frames in § 2.1, we take those for $(\hat{U}_\xi, \hat{U}_\eta, \hat{U}_\phi)$ and $(\hat{u}_\xi, \hat{u}_\eta)$ viewed from the plane wall for convenience of the simulations. Consequently, $\hat{U}_\xi = \hat{U}_\eta = \hat{U}_\phi = \hat{u}_\xi = \hat{u}_\eta = 0$ on the plane wall and on the boundary sufficiently far from the bubble.

We follow a conventional staggered grid arrangement (Harlow & Welch 1965), where the velocity component is located on the corresponding cell interface, and the pressure at the cell centre, as shown in figure 9(*b*). The basic equations are discretized by the second-order finite-difference scheme. To numerically guarantee the mass and momentum conservations, and to accurately conduct the numerical integration in computing the drag and migration forces, we use the exact values of the grid width, the cell interfacial area and the control volume in the bipolar coordinates. To this end, for the integral of the scale factors

$$g_\xi(\xi,\eta) = \int_\alpha^\xi \mathrm{d}\bar{\xi}\; h_\xi(\bar{\xi},\eta), \quad g_{\xi\phi}(\xi,\eta) = \int_\alpha^\xi \mathrm{d}\bar{\xi}\; h_\xi(\bar{\xi},\eta) h_\phi(\bar{\xi},\eta), \tag{A 6}$$

$$g_\eta(\xi,\eta) = \int_\pi^\eta \mathrm{d}\bar{\eta}\; h_\eta(\xi,\bar{\eta}), \quad g_{\eta\phi}(\xi,\eta) = \int_\pi^\eta \mathrm{d}\bar{\eta}\; h_\eta(\xi,\bar{\eta}) h_\phi(\xi,\bar{\eta}), \tag{A 7}$$

$$g_{\xi\eta}(\xi,\eta) = \int_\alpha^\xi \mathrm{d}\bar{\xi} \int_\pi^\eta \mathrm{d}\bar{\eta}\; h_\xi(\bar{\xi},\bar{\eta}) h_\eta(\bar{\xi},\bar{\eta}), \quad g(\xi,\eta) = \int_\alpha^\xi \mathrm{d}\bar{\xi} \int_\pi^\eta \mathrm{d}\bar{\eta}\; h(\bar{\xi},\bar{\eta}), \tag{A 8}$$

we use the exact expressions

$$g_\xi = \frac{2k}{\sin\eta}\left(\tan^{-1}\left(\frac{\mathscr{D}+\mathscr{C}}{\mathscr{S}}\right) - \tan^{-1}\left(\frac{\mathscr{D}_\alpha+\mathscr{C}_\alpha}{\mathscr{S}_\alpha}\right)\right), \tag{A 9}$$

$$g_\eta = -\frac{2k}{\sinh\xi}\tan^{-1}\left(\frac{\mathscr{D}+\mathscr{C}}{\mathscr{S}}\right), \tag{A 10}$$

$$\begin{aligned} g_{\xi\eta} = k^2\bigg\{ &\left(\frac{1}{\sinh^2\xi} - \frac{1}{\sin^2\eta}\right)\tan^{-1}\left(\frac{\mathscr{D}+\mathscr{C}}{\mathscr{S}}\right) \\ &- \left(\frac{1}{\sinh^2\alpha} - \frac{1}{\sin^2\eta}\right)\tan^{-1}\left(\frac{\mathscr{D}_\alpha+\mathscr{C}_\alpha}{\mathscr{S}_\alpha}\right) - \left(\frac{\mathscr{C}+2}{2\mathscr{S}} - \frac{\mathscr{C}_\alpha+2}{2\mathscr{S}_\alpha}\right)\bigg\}, \end{aligned} \tag{A 11}$$

$$g_{\eta\phi} = k^2\left(-\frac{1}{\mathscr{D}} + \frac{1}{\cosh\xi + 1}\right), \tag{A 12}$$

$$g_{\xi\phi} = k^2\left\{\frac{2\cos\eta}{\sin^2\eta}\left(\tan^{-1}\left(\frac{\mathscr{D}+\mathscr{C}}{\mathscr{S}}\right) - \tan^{-1}\left(\frac{\mathscr{D}_\alpha+\mathscr{C}_\alpha}{\mathscr{S}_\alpha}\right)\right) + \frac{\sinh\xi}{\mathscr{D}\sin\eta} - \frac{\sinh\alpha}{\mathscr{D}_\alpha\sin\eta}\right\}, \tag{A 13}$$

$$\begin{aligned} g = &-\frac{k^3}{\sin^3\eta}\left\{\left(\tan^{-1}\left(\frac{\mathscr{D}+\mathscr{C}}{\mathscr{S}}\right) - \tan^{-1}\left(\frac{\mathscr{D}_\alpha+\mathscr{C}_\alpha}{\mathscr{S}_\alpha}\right)\right)\cos\eta + \frac{\mathscr{S}}{2\mathscr{D}} - \frac{\mathscr{S}_\alpha}{2\mathscr{D}_\alpha}\right\} \\ &-\frac{k^3}{12}\left(\tanh^3\frac{\xi}{2} - \tanh^3\frac{\alpha}{2}\right) + \frac{k^3}{4}\left(\tanh\frac{\xi}{2} - \tanh\frac{\alpha}{2}\right), \end{aligned} \tag{A 14}$$

where

$$\left.\begin{aligned} h = h_\xi h_\eta h_\phi, \quad \mathscr{C} = \cosh\xi\cos\eta - 1, \quad \mathscr{S} = \sinh\xi\sin\eta, \\ \mathscr{D}_\alpha = \cosh\alpha - \cos\eta, \quad \mathscr{C}_\alpha = \cosh\alpha\cos\eta - 1, \quad \mathscr{S}_\alpha = \sinh\alpha\sin\eta. \end{aligned}\right\} \tag{A 15}$$

We introduce the finite-difference operators δ_i and δ_j, of which the indices i and j correspond to discretized coordinates along the respective directions ξ and η, such as

$$\left.\begin{aligned} \delta_i(q)|_{i,j} &= q_{i+1/2,j} - q_{i-1/2,j}, \\ \delta_j(q)|_{i,j} &= q_{i,j+1/2} - q_{i,j-1/2}, \\ \delta_i\delta_j(q)|_{i,j} &= q_{i+1/2,j+1/2} - q_{i+1/2,j-1/2} - q_{i-1/2,j+1/2} + q_{i-1/2,j-1/2}. \end{aligned}\right\} \tag{A 16}$$

Using these operators, we write the divergence of the velocity vector $\boldsymbol{U}$ in (2.1) as

$$\left.\widehat{\nabla\cdot\boldsymbol{U}}\right|_{i,j}\left(\equiv\frac{\nabla\cdot\boldsymbol{U}}{\cos\phi}\right) = \frac{(\delta_i(\delta_j(g_{\eta\phi})\hat{U}_\xi)|_{i,j} + \delta_j(\delta_i(g_{\xi\phi})\hat{U}_\eta)|_{i,j} + \hat{U}_\phi\delta_i\delta_j(g_{\xi\eta})|_{i,j})}{\delta_i\delta_j(g)|_{i,j}}, \tag{A 17}$$

and the components of the Stokes equation (2.2) for the bubble translating parallel to the plane wall as

$$\left.\begin{aligned} 0 &= \frac{\delta_i(-\hat{P} + \widehat{\nabla\cdot\boldsymbol{U}})|_{i+1/2,j}}{\delta_i(g_\xi)|_{i+1/2,j}} + \frac{-\delta_j(r\hat{\varOmega}_\phi)|_{i+1/2,j} + \hat{\varOmega}_\eta\delta_j(g_\eta)|_{i+1/2,j}}{\delta_j(g_{\eta\phi})|_{i+1/2,j}}, \\ 0 &= \frac{\delta_j(-\hat{P} + \widehat{\nabla\cdot\boldsymbol{U}})|_{i,j+1/2}}{\delta_j(g_\eta)|_{i,j+1/2}} + \frac{\delta_i(r\hat{\varOmega}_\phi)|_{i,j+1/2} - \hat{\varOmega}_\xi\delta_i(g_\xi)|_{i,j+1/2}}{\delta_i(g_{\xi\phi})|_{i,j+1/2}}, \\ 0 &= \frac{(\hat{P} - \widehat{\nabla\cdot\boldsymbol{U}})|_{i,j}}{r|_{i,j}} + \frac{-\delta_i(\delta_j(g_\eta)\hat{\varOmega}_\eta)|_{i,j} + \delta_j(\delta_i(g_\xi)\hat{\varOmega}_\xi)|_{i,j}}{\delta_i\delta_j(g_{\xi\eta})|_{i,j}}, \end{aligned}\right\} \tag{A 18}$$

where $\hat{\varOmega}$ denotes the vorticity, of which each component is

$$\left.\begin{aligned} \hat{\varOmega}_\xi|_{i,j+1/2} &= \frac{\delta_j(r\hat{U}_\phi)|_{i,j+1/2} + \hat{U}_\eta\delta_j(g_\eta)|_{i,j+1/2}}{\delta_j(g_{\eta\phi})|_{i,j+1/2}}, \\ \hat{\varOmega}_\eta|_{i+1/2,j} &= \frac{-\delta_i(r\hat{U}_\phi)|_{i+1/2,j} - \hat{U}_\xi\delta_i(g_\xi)|_{i+1/2,j}}{\delta_i(g_{\xi\phi})|_{i+1/2,j}}, \\ \hat{\varOmega}_\phi|_{i+1/2,j+1/2} &= \frac{\delta_i(\delta_j(g_\eta)\hat{U}_\eta)|_{i+1/2,j+1/2} - \delta_j(\delta_i(g_\xi)\hat{U}_\xi)|_{i+1/2,j+1/2}}{\delta_i\delta_j(g_{\xi\eta})|_{i+1/2,j+1/2}}. \end{aligned}\right\} \tag{A 19}$$

Replacing $\hat{U}_\xi$, $\hat{U}_\eta$ and $\hat{P}$, respectively, by $\hat{u}_\xi$, $\hat{u}_\eta$ and p with $\hat{U}_\phi = \hat{\varOmega}_\xi = \hat{\varOmega}_\eta = 0$, we readily obtain the governing equation for the field $(\hat{u}_\xi, \hat{u}_\eta, \hat{p})$. We write the kinematic and free-slip conditions (2.4) as

$$\hat{U}_\xi|_{N_\alpha+1/2,j} = \widehat{\boldsymbol{e}_r \cdot \boldsymbol{e}_\xi}|_{N_\alpha+1/2,j}, \quad \hat{u}_\xi|_{N_\alpha+1/2,j} = -\boldsymbol{e}_z \cdot \boldsymbol{e}_\xi|_{N_\alpha+1/2,j}, \tag{A 20}$$

$$\hat{\Sigma}_{\xi\eta}|_{N_\alpha+1/2,j+1/2} = \hat{\Sigma}_{\xi\phi}|_{N_\alpha+1/2,j} = \hat{\sigma}_{\xi\eta}|_{N_\alpha+1/2,j+1/2} = 0, \tag{A 21}$$

where the index $N_\alpha + 1/2$ denotes the node at the bubble surface $\xi = \alpha$,

$$\widehat{\boldsymbol{e}_r \cdot \boldsymbol{e}_\xi} = \frac{\delta_j\left(g^{(\xi)}_{\xi\eta}\right)}{\delta_j(g_{\eta\phi})}, \quad \boldsymbol{e}_z \cdot \boldsymbol{e}_\xi = -\frac{\delta_j(r^2)}{2\delta_j(g_{\eta\phi})}, \tag{A 22}$$

$$g^{(\xi)}_{\xi\eta} = \int_{\pi}^{\eta} \mathrm{d}\bar{\eta} \left(-\frac{k^2 \mathscr{S} \sin\bar{\eta}}{\mathscr{D}^3}\right) = k^2 \left\{ \frac{1}{\sinh^2\xi} \tan^{-1}\left(\frac{\mathscr{D}+\mathscr{C}}{\mathscr{S}}\right) + \frac{\mathscr{C}\sin\eta}{2\mathscr{D}^2 \sinh\xi} \right\}, \tag{A 23}$$

$$\hat{\Sigma}_{\xi\eta} = \frac{1}{\delta_i\delta_j(g_{\xi\eta})} \left\{ \overline{\delta_i(g_\xi)}^j \delta_j(\hat{U}_\xi) - \delta_i\delta_j(g_\xi)\overline{\hat{U}_\xi}^j + \overline{\delta_j(g_\eta)}^i \delta_i(\hat{U}_\eta) - \delta_i\delta_j(g_\eta)\overline{\hat{U}_\eta}^i \right\}, \tag{A 24}$$

$$\hat{\Sigma}_{\xi\phi} = \frac{1}{\delta_i(g_{\xi\phi})} \left\{ \overline{r}^i \delta_i(\hat{U}_\phi) - \delta_i(r)\overline{\hat{U}_\phi}^i - \delta_i(g_\xi)\hat{U}_\xi \right\}, \tag{A 25}$$

$$\hat{\sigma}_{\xi\eta} = \frac{1}{\delta_i\delta_j(g_{\xi\eta})} \left\{ \overline{\delta_i(g_\xi)}^j \delta_j(\hat{u}_\xi) - \delta_i\delta_j(g_\xi)\overline{\hat{u}_\xi}^j + \overline{\delta_j(g_\eta)}^i \delta_i(\hat{u}_\eta) - \delta_i\delta_j(g_\eta)\overline{\hat{u}_\eta}^i \right\}, \tag{A 26}$$

and the overline stands for the interpolation such as

$$\overline{q}^i|_{i,j} = \frac{q_{i+1/2,j} + q_{i-1/2,j}}{2}, \quad \overline{q}^j|_{i,j} = \frac{q_{i,j+1/2} + q_{i,j-1/2}}{2}. \tag{A 27}$$

We write the area integral on the bubble surface in a summation form,

$$\oint_{S_B} \mathrm{d}\boldsymbol{x}^2\, q \equiv \int_0^{2\pi} \mathrm{d}\phi \int_0^{\pi} \mathrm{d}\eta\ h_\eta h_\phi\ q|_{\xi=\alpha} = \sum_{j=1}^{N_j} \left(\delta_j(g_{\eta\phi}) \int_0^{2\pi} \mathrm{d}\phi\ q \right)_{N_\alpha+1/2,j}, \tag{A 28}$$

where N_j is the number of grid points in the η direction. The drag force F_{DC} in (2.10) is given by

$$F_{DC} = 2\pi \sum_{j=1}^{N_j} \left(\delta_j(g_{\eta\phi}) \boldsymbol{e}_z \cdot \boldsymbol{e}_\xi \overline{\hat{\sigma}_{\xi\xi}}^i \right)_{N_\alpha+1/2,j}, \tag{A 29}$$

where

$$\hat{\sigma}_{\xi\xi} = -\hat{p} + \frac{2\overline{\delta_j(g_{\eta\phi})}^i \delta_i(\hat{u}_\xi)}{\delta_i\delta_j(g)} + \frac{2\overline{r}^j \delta_i\delta_j(g_\xi)\overline{\hat{u}_\eta}^j}{\delta_i\delta_j(g)}. \tag{A 30}$$

For the deflection $\hat{f} = f^{(Ca)}/(a\cos\phi)$, the Laplace law (2.3) is expressed as

$$a^{(f)}_{n,j}\hat{f}|_{j+1} + a^{(f)}_{s,j}\hat{f}|_{j-1} - a^{(f)}_{p,j}\hat{f}|_j = S^{(f)}|_j, \tag{A 31}$$

where

$$\left.\begin{aligned} a^{(f)}_{n,j} &= \frac{r_{N_\alpha+1/2,j+1/2}}{\overline{\delta_j(g_\eta)}^i|_{N_\alpha+1/2,j+1/2}\delta_j(g_{\eta\phi})|_{N_\alpha+1/2,j}}, \\ a^{(f)}_{s,j} &= \frac{r_{N_\alpha+1/2,j-1/2}}{\overline{\delta_j(g_\eta)}^i|_{N_\alpha+1/2,j-1/2}\delta_j(g_{\eta\phi})|_{N_\alpha+1/2,j}}, \\ a^{(f)}_{p,j} &= \frac{a^{(f)}_{n,j}(\widehat{\boldsymbol{e}_r \cdot \boldsymbol{e}_\xi})_{N_\alpha+1/2,j+1} + a^{(f)}_{s,j}(\widehat{\boldsymbol{e}_r \cdot \boldsymbol{e}_\xi})_{N_\alpha+1/2,j-1}}{(\widehat{\boldsymbol{e}_r \cdot \boldsymbol{e}_\xi})_{N_\alpha+1/2,j}}, \end{aligned}\right\}, \tag{A 32}$$

$$S^{(f)} = -\overline{\hat{\Sigma}_{\xi\xi}}^{i} + \frac{\widehat{\boldsymbol{e}_r\boldsymbol{\cdot}\boldsymbol{e}_\xi}\sum_{j=1}^{N_j}(\delta_j(g_{\eta\phi})\widehat{\boldsymbol{e}_r\boldsymbol{\cdot}\boldsymbol{e}_\xi}\,\overline{\hat{\Sigma}_{\xi\xi}}^{i})_j}{\sum_{j=1}^{N_j}(\delta_j(g_{\eta\phi})\widehat{\boldsymbol{e}_r\boldsymbol{\cdot}\boldsymbol{e}_\xi})_j^2}, \tag{A 33}$$

$$\hat{\Sigma}_{\xi\xi} = -\hat{P} + \frac{2\overline{\delta_j(g_{\eta\phi})}^{i}\,\delta_i(\hat{U}_\xi)}{\delta_i\delta_j(g)} + \frac{2\overline{r}^{j}\,\delta_i\delta_j(g_\xi)\overline{\hat{U}_\eta}^{j}}{\delta_i\delta_j(g)}. \tag{A 34}$$

The deformation-induced lateral force $F_M^{(Ca)}$ in (2.7) is given by

$$\begin{aligned} F_M^{(Ca)} = \pi\sum_j\Bigg[& \frac{\delta_j(g_{\eta\phi})\overline{\hat{\sigma}_{\xi\xi}}^{i}\,\delta_i(\hat{U}_\xi - \widehat{\boldsymbol{e}_r\boldsymbol{\cdot}\boldsymbol{e}_\xi})\hat{f}}{\delta_i(g_\xi)} + \frac{r\delta_i\delta_j(g_\xi)\overline{\overline{\hat{\sigma}_{\xi\xi}}^{i}}^{j}\,\overline{(\hat{U}_\eta - \widehat{\boldsymbol{e}_r\boldsymbol{\cdot}\boldsymbol{e}_\eta})}^{i}\,\overline{\hat{f}}^{j}}{\overline{\delta_i(g_\xi)}^{j}} \\ & + \delta_j(g_{\eta\phi})\overline{\hat{\sigma}_{\xi\xi}}^{i}\,\overline{\left(\frac{(\hat{U}_\phi+1)}{r}\right)}^{i}\hat{f} - r\overline{\overline{\hat{\sigma}_{\xi\xi}}^{i}}^{j}\,\overline{(\hat{U}_\eta - \widehat{\boldsymbol{e}_r\boldsymbol{\cdot}\boldsymbol{e}_\eta})}^{i}\,\delta_j(\hat{f}) \\ & - \frac{\overline{\delta_j(g_{\eta\phi})}^{j}\,\overline{(\hat{u}_\eta + \boldsymbol{e}_z\boldsymbol{\cdot}\boldsymbol{e}_\eta)}^{i}\,\delta_i(\hat{\Sigma}_{\xi\eta})\overline{\hat{f}}^{j}}{\delta_i(g_\xi)} + \frac{r\delta_i\delta_j(g_\xi)\overline{(\hat{u}_\eta + \boldsymbol{e}_z\boldsymbol{\cdot}\boldsymbol{e}_\eta)}^{i}}{\overline{\delta_i(g_\xi)}^{j}}\left(\overline{\overline{\hat{\Sigma}_{\xi\xi}}^{i}}^{j} - \overline{\overline{\hat{\Sigma}_{\eta\eta}}^{i}}^{j}\right)\overline{\hat{f}}^{j} \\ & + r\overline{(\hat{u}_\eta + \boldsymbol{e}_z\boldsymbol{\cdot}\boldsymbol{e}_\eta)}^{i}\,\overline{\overline{\hat{\Sigma}_{\eta\eta}}^{i}}^{j}\,\delta_j(\hat{f}) - \frac{\overline{(\hat{u}_\eta + \boldsymbol{e}_z\boldsymbol{\cdot}\boldsymbol{e}_\eta)}^{i}}{r}\,\overline{(\delta_j(g_{\eta\phi})\hat{\Sigma}_{\eta\phi})}^{i}\,\overline{\hat{f}}^{j} \\ & + r\overline{(\hat{u}_\eta + \boldsymbol{e}_z\boldsymbol{\cdot}\boldsymbol{e}_\eta)}^{i}\,\overline{S^{(f)}}^{j}\,\delta_j(\hat{f})\Bigg]_{N_\alpha+1/2}, \end{aligned} \tag{A 35}$$

where

$$\widehat{\boldsymbol{e}_r\boldsymbol{\cdot}\boldsymbol{e}_\eta} = \frac{\delta_i(g_{\xi\eta}^{(\eta)})}{\delta_i(g_{\xi\phi})}, \quad \boldsymbol{e}_z\boldsymbol{\cdot}\boldsymbol{e}_\eta = \frac{\delta_i(r^2)}{2\delta_i(g_{\xi\phi})}, \tag{A 36}$$

$$\begin{aligned} g_{\xi\eta}^{(\eta)} = \int_\alpha^\xi \mathrm{d}\bar{\xi}\,\frac{k^2\mathscr{C}\sin\eta}{\mathscr{D}^3} = k^2\Bigg\{ & -\frac{1}{\sin^2\eta}\left(\tan^{-1}\left(\frac{\mathscr{D}+\mathscr{C}}{\mathscr{S}}\right) - \tan^{-1}\left(\frac{\mathscr{D}_\alpha+\mathscr{C}_\alpha}{\mathscr{S}_\alpha}\right)\right) \\ & - \left(\frac{\mathscr{C}+2}{2\mathscr{S}} - \frac{\mathscr{C}_\alpha+2}{2\mathscr{S}_\alpha}\right) - \left(\frac{\mathscr{C}\sin\eta}{2\mathscr{D}^2\sinh\xi} - \frac{\mathscr{C}_\alpha\sin\eta}{2\mathscr{D}_\alpha^2\sinh\alpha}\right)\Bigg\}, \end{aligned} \tag{A 37}$$

$$\hat{\Sigma}_{\eta\eta} = -\hat{P} + \frac{2\overline{\delta_i(g_{\xi\phi})}^{j}\,\delta_j(\hat{U}_\eta)}{\delta_i\delta_j(g)} + \frac{2\overline{r}^{i}\,\delta_i\delta_j(g_\eta)\overline{\hat{U}_\xi}^{i}}{\delta_i\delta_j(g)}, \tag{A 38}$$

$$\hat{\Sigma}_{\eta\phi} = \frac{1}{\delta_j(g_{\eta\phi})}\left\{\overline{r}^{j}\delta_j(\hat{U}_\phi) - \delta_j(r)\overline{\hat{U}_\phi}^{j} - \delta_j(g_\eta)\hat{U}_\eta\right\}. \tag{A 39}$$

Appendix B. Small deformation theory in the lubrication limit

The governing equations for $\hat{U}_r^{(0)}$, $\hat{U}_\phi^{(0)}$, $\hat{U}_z^{(0)}$, $\hat{P}^{(0)}$, $\hat{U}_r^{(f)}$, $\hat{U}_z^{(f)}$ and $\hat{P}^{(f)}$ in (2.17)–(2.21) are written as

$$\frac{1}{R}\frac{\partial(R\hat{U}_r^{(0)})}{\partial R} + \frac{\hat{U}_\phi^{(0)}}{R} + \frac{\partial\hat{U}_z^{(0)}}{\partial Z} = \frac{1}{R}\frac{\partial(R\hat{U}_r^{(f)})}{\partial R} + \frac{\partial\hat{U}_z^{(f)}}{\partial Z} = 0, \tag{B 1}$$

$$-\frac{\partial \hat{P}^{(0)}}{\partial R}+\frac{\partial^2 \hat{U}_r^{(0)}}{\partial Z^2}=\frac{\hat{P}^{(0)}}{R}+\frac{\partial^2 \hat{U}_\phi^{(0)}}{\partial Z^2}=\frac{\partial \hat{P}^{(0)}}{\partial Z}$$
$$=-\frac{\partial \hat{P}^{(f)}}{\partial R}+\frac{\partial^2 \hat{U}_r^{(f)}}{\partial Z^2}=\frac{\partial \hat{P}^{(f)}}{\partial Z}=0, \tag{B 2}$$

with the no-slip boundary condition on the plane wall

$$\boldsymbol{u}=0 \quad \text{at} \quad Z=0, \tag{B 3}$$

and the free-slip and kinematic boundary conditions on the bubble surface. The deformed interface is located on the curve where $H-\delta\hat{F}\cos\phi-Z=0$ holds. From this relation, the normal unit vector $\boldsymbol{n}$ pointing outwards from the liquid on the bubble surface is approximated by

$$\boldsymbol{n}(R,\phi)=-\boldsymbol{e}_z+\boldsymbol{e}_r\varepsilon^{1/2}\left(R-\delta\frac{\mathrm{d}\hat{F}}{\mathrm{d}R}\cos\phi\right)+\boldsymbol{e}_\phi\varepsilon^{1/2}\delta\frac{\hat{F}}{R}\sin\phi+\cdots. \tag{B 4}$$

Applying the Taylor expansion to a function $q=q^{(0)}+\delta\ q^{(f)}+\cdots$ in terms of the deflection around the undeformed interface, one obtains a relation on the deformed interface $Z=H-\delta\hat{F}\cos\phi$

$$q|_{interface}=q|_{Z=H}^{(0)}+\delta\left(-\hat{F}\cos\phi\left.\frac{\partial q^{(0)}}{\partial Z}\right|_{Z=H}+q|_{Z=H}^{(f)}\right)+\cdots. \tag{B 5}$$

Taking (B 4) and (B 5) into account, one writes the kinematic condition on the bubble surface as

$$R\hat{U}_r^{(0)}-\hat{U}_z^{(0)}-R=R\hat{U}_r^{(f)}-\hat{U}_z^{(f)}-\frac{1}{2}\frac{\mathrm{d}\hat{F}}{\mathrm{d}R}\hat{U}_r^{(0)}+\frac{\hat{F}}{2R}\hat{U}_\phi^{(0)}-\frac{\hat{F}R}{2}\frac{\partial\hat{U}_r^{(0)}}{\partial Z}$$
$$+\frac{\hat{F}}{2}\frac{\partial\hat{U}_z^{(0)}}{\partial Z}+\frac{1}{2}\left(\frac{\mathrm{d}\hat{F}}{\mathrm{d}R}+\frac{\hat{F}}{R}\right)=0 \quad \text{at} \quad Z=H, \tag{B 6}$$

and the free-slip boundary condition as

$$\frac{\partial\hat{U}_r^{(0)}}{\partial Z}=\frac{\partial\hat{U}_\phi^{(0)}}{\partial Z}=\frac{\partial\hat{U}_r^{(f)}}{\partial Z}-\frac{\hat{F}}{2}\frac{\partial^2\hat{U}_r^{(0)}}{\partial Z^2}=0 \quad \text{at} \quad Z=H. \tag{B 7}$$

The vertical drag force acting on the bubble, which is involved in the second term in the right-hand side of (2.3), is of order $\log\varepsilon$, as determined for a motion of a rigid sphere (Goldman *et al.* 1967; O'Neill & Stewartson 1967) by means of the matched asymptotic expansion technique, and the normal stress on the bubble surface is dominated by the pressure $p=O(\varepsilon^{-3/2})$, as compared with $\partial_r u_r=O(\varepsilon^{-1/2})$, $u_r/r=O(\varepsilon^{-1/2})$, $u_\phi/r=O(\varepsilon^{-1/2})$ and $\partial_z u_z=O(\varepsilon^{-1/2})$, which are related to the viscous stresses. Hence, the Laplace law (2.3) is simplified to

$$\frac{\mathrm{d}}{\mathrm{d}R}\left(\frac{1}{R}\frac{\mathrm{d}(R\hat{F})}{\mathrm{d}R}\right)=\hat{P}^{(0)}, \tag{B 8}$$

with no singularity conditions $\hat{F}=0$ at $R=0$ and $\hat{F}\to 0$ as $R\to\infty$.

As obtained by Hodges *et al.* (2004), the leading-order and perturbed solutions are

$$\left.\begin{aligned} \hat{U}_r^{(0)} &= \frac{(6-9R^2)}{20H}\left(\frac{Z^2}{H^2}-\frac{2Z}{H}\right), \quad \hat{U}_\phi^{(0)} = -\frac{3}{10}\left(\frac{Z^2}{H^2}-\frac{2Z}{H}\right), \\ \hat{U}_z^{(0)} &= \frac{(4R-R^3)Z^3}{5H^4} + \frac{(-42R+3R^3)Z^2}{20H^3}, \end{aligned}\right\} \tag{B 9}$$

$$\hat{P}^{(0)} = \frac{3R}{5H^2}, \tag{B 10}$$

$$\hat{F} = -\frac{3\log H}{5R}. \tag{B 11}$$

$$\left.\begin{aligned} \hat{U}_r^{(f)}(R,Z) &= A_2(R)Z^2 + A_1(R)Z, \\ \hat{U}_z^{(f)}(R,Z) &= -\frac{1}{3R}\frac{\mathrm{d}(RA_2)}{\mathrm{d}R}Z^3 - \frac{1}{2R}\frac{\mathrm{d}(RA_1)}{\mathrm{d}R}Z^2, \end{aligned}\right\} \tag{B 12}$$

$$\hat{P}^{(f)}(R) = \textstyle\int_\infty^R \mathrm{d}\bar{R}\ 2A_2(\bar{R}), \tag{B 13}$$

where

$$A_1 = \frac{9(14-R^2)\log H}{100H^3R}, \tag{B 14}$$

$$A_2 = -\frac{9(4-R^2)\log H}{50H^4R}. \tag{B 15}$$

Substituting (B 15) into (B 13) estimates the asymptotic order of the perturbed pressure

$$\varepsilon^{-3/2}\delta\hat{P}^{(f)} = \frac{12\varepsilon^{-3}Ca\log(R^2/2)}{25R^6} + O(R^{-6}) \quad \text{for} \quad R \gg 1, \tag{B 16}$$

which is $O(Ca\log\varepsilon\ (\varepsilon^{1/2}R)^{-6})$ in the overlapping region $R \sim \varepsilon^{-1/2}$, and thus to be matched with the pressure of $O(Ca\log\varepsilon\ r^{-6})$ in the outer region (O'Neill & Stewartson 1967). This outer pressure may contribute to the lateral force of $O(Ca\log\varepsilon)$, which is larger than that for the wide-gap case, corresponding to $O(Ca)$. Nevertheless, as discussed in Urzay *et al.* (2007), the rapid decay of the perturbed pressure for $R \gg 1$ indicates that the contribution of the outer pressure to the lateral force is negligibly smaller than that of the inner pressure. Therefore, to evaluate the leading-order migration force, one does not have to solve the outer problem. (In fact, the order of the lateral force (B 20) evaluated only in the inner region is confirmed to be $O(Ca\varepsilon^{-2})$ and larger than the outer contribution $O(Ca\log\varepsilon)$.) The leading pressure $\varepsilon^{-3/2}\hat{P}^{(0)}\cos\phi$ with no deformation is locally dominant but does not contribute to the lateral force due to its azimuthal cosine dependence. The viscous stress contribution to the lateral force is $O(\varepsilon)$ smaller than the pressure in the inner region. The deformation-induced lateral force F_M to cancel the migration velocity and to maintain the wall-parallel motion is expressed as

$$F_M \approx \oint_{contact} \mathrm{d}^2\boldsymbol{x}\ \varepsilon^{-3/2}\delta\hat{P}^{(f)}. \tag{B 17}$$

The surface integral for a function q on the contact side is taken from the axis $R=0$ to the overlapping region, i.e.

$$\oint_{contact} \mathrm{d}^2\boldsymbol{x}\ q = \varepsilon\int_0^{2\pi}\mathrm{d}\phi\int_0^{\mathfrak{R}}\mathrm{d}R\ R\ q(R,\phi), \tag{B 18}$$

where $\mathfrak{R} = O(\varepsilon^{-1/2})$. For $\mathfrak{R} \gg 1$, one obtains an asymptotic relation

$$\int_0^{\mathfrak{R}} \mathrm{d}R\ R\ \hat{P}^{(f)}(R) = -\int_0^{\mathfrak{R}} \mathrm{d}R\ R^2 A_2(R) - \mathfrak{R}^2 \int_{\mathfrak{R}}^{\infty} \mathrm{d}R\ A_2(R)$$

$$= \frac{3}{100} + \frac{6\log(\mathfrak{R}^2/2)}{25\mathfrak{R}^4} + \frac{1}{5\mathfrak{R}^4} + O(\mathfrak{R}^{-6}\log\mathfrak{R}) \qquad \text{(B 19)}$$

of which only the first term does not vanish as $\mathfrak{R} \to \infty$. As obtained by Hodges *et al.* (2004), consequently, the asymptotic solution of the deformation-induced lateral force in the lubrication limit is

$$F_M \to \lim_{\mathfrak{R}\to\infty} \varepsilon \int_0^{2\pi} \mathrm{d}\phi \int_0^{\mathfrak{R}} \mathrm{d}R\ R\ \varepsilon^{-3/2}\delta\hat{P}^{(f)}(R)$$

$$= \frac{3\pi Ca}{50}\varepsilon^{-2} \quad \text{as} \quad \varepsilon \to 0. \qquad \text{(B 20)}$$

REFERENCES

Amsden, A. A. & Harlow, F. H. 1970 A simplified MAC technique for incompressible fluid flow calculations. *J. Comput. Phys.* **6**, 322–325.

Bart, E. 1968 The slow unsteady settling of a fluid sphere toward a flat fluid interface. *Chem. Engng Sci.* **23**, 193–210.

Batchelor, G. K. 1967 *An Introduction to Fluid Dynamics*. Cambridge University Press.

Becker, L. E., McKinley, G. H. & Stone, H. A. 1996 Sedimentation of a sphere near a plane wall: weak non-Newtonian and inertial effects. *J. Non-Newton. Fluid Mech.* **63**, 201–233.

Callens, N., Minetti, C., Coupier, G., Mader, M.-A., Dubois, F., Misbah, C. & Podgorski, T. 2008 Hydrodynamic lift of vesicles under shear flow in microgravity. *Europhys. Lett.* **83**, 24002.

Chaffey, C. E., Brenner, H. & Mason, S. G. 1965 Particle motions in sheared suspensions. Part XVIII. Wall migration (theoretical). *Rheol. Acta* **4**, 64–72 (correction in *Rheol. Acta* **6**, 100).

Chan, P. C.-H. & Leal, L. G. 1979 The motion of a deformable drop in a second-order fluid. *J. Fluid Mech.* **92**, 131–170.

Cherukat, P. & McLaughlin, J. B. 1994 The inertial lift on a rigid sphere in a linear shear flow field near a flat wall. *J. Fluid Mech.* **263**, 1–18.

Correas, J.-M., Bridal, L., Lesavre, A., Méjean, A., Claudon, M. & Hélénon, O. 2001 Ultrasound contrast agents: properties, principles of action, tolerance, and artifacts. *Eur. Radiol.* **11**, 1316–1328.

Cox, R. G. & Brenner, H. 1968 The lateral migration of solid particles in Poiseuille flow. Part I. Theory. *Chem. Engng Sci.* **23**, 147–173.

Cox, R. G. & Hsu, S. K. 1977 The lateral migration of solid particles in a laminar flow near a plane. *Intl J. Multiph. Flow* **3**, 201–222.

Dimitrakopoulos, P. 2007 Interfacial dynamics in Stokes flow via a three-dimensional fully-implicit interfacial spectral boundary element algorithm. *J. Comput. Phys.* **225**, 408–426.

Fukagata, K. & Kasagi, N. 2002 Highly energy-conservative finite difference method for the cylindrical coordinate system. *J. Comput. Phys.* **181**, 478–498.

Garstecki, P., Fuerstman, M. J., Stone, H. A. & Whitesides, G. M. 2006 Formation of droplets and bubbles in a microfluidic T-junction-scaling and mechanism of break-up. *Lab on a Chip* **6**, 437–446.

Goldman, A. J., Cox, R. G. & Brenner, H. 1967 Slow viscous motion of a sphere parallel to a plane wall-I motion through a quiescent fluid. *Chem. Engng Sci.* **22**, 637–651.

Happel, J. & Brenner, H. 1973 *Low Reynolds Number Hydrodynamics*, 2nd edn. Martinus Nijhoff.

Harlow, F. H. & Welch, J. E. 1965 Numerical calculation of time-dependent viscous incompressible flow of fluid with free surface. *Phys. Fluids* **8**, 2182–2189.

Hibiki, T. & Ishii, M. 2007 Lift force in bubbly flow systems. *Chem. Engng Sci.* **62**, 6457–6472.

Ho, B. P. & Leal, L. G. 1974 Inertial migration of rigid spheres in two-dimensional unidirectional flows. *J. Fluid Mech.* **65**, 365–400.

Hodges, S. R., Jensen, O. E. & Rallison, J. M. 2004 Sliding, slipping and rolling: the sedimentation of a viscous drop down a gently inclined plane. *J. Fluid Mech.* **512**, 95–131.

Leal, L. G. 1980 Particle motions in a viscous fluid. *Annu. Rev. Fluid Mech.* **12**, 435–476.

Leal, L. G. 1992 *Laminar Flow and Convective Transport Processes.* Butterworth-Heinemann.

Magnaudet, J., Takagi, S. & Legendre, D. 2003 Drag, deformation and lateral migration of a buoyant drop moving near a wall. *J. Fluid Mech.* **476**, 115–157.

Makuta, T., Takemura, F., Hihara, E., Matsumoto, Y. & Shoji, M. 2006 Generation of micro gas bubbles of uniform diameter in an ultrasonic field. *J. Fluid Mech.* **548**, 113–131.

McLaughlin, J. B. 1993 The lift on a small sphere in wall-bounded linear shear flows. *J. Fluid Mech.* **246**, 249–265.

Olla, P. 1997 The lift on a tank-treading ellipsoidal cell in a shear flow. *J. Phys.* II *France* **7**, 1533–1540.

O'Neill, M. E. 1964 A slow motion of viscous liquid caused by a slowly moving solid sphere. *Mathematika* **11**, 67–74.

O'Neill, M. E. & Stewartson, K. 1967 On the slow motion of a sphere parallel to a nearby plane wall. *J. Fluid Mech.* **27**, 705–724.

Sekimoto, K. & Leibler, L. 1993 A mechanism for shear thickening of polymer-bearing surfaces: elasto-hydrodynamic coupling. *Europhys. Lett.* **23**, 113–117.

Serizawa, A., Inui, T., Yahiro, T. & Kawara, Z. 2005 Pseudo-laminarizaion of micro-bubble containing milky bubbly flow in a pipe. *Multiph. Sci. Tech.* **17**, 79–101.

Shapira, M. & Haber, S. 1988 Low Reynolds number motion of a droplet between two parallel plates. *Intl J. Multiph. Flow* **14**, 483–506.

Shortencarier, M. J., Dayton, P. A., Bloch, S. H., Schumann, P. A., Matsunaga, T. O. & Ferrara, K. W. 2004 A method for radiation-force localized drug delivery using gas-filled lipospheres. *IEEE Trans. Ultrason. Ferroelectr. Freq. Control* **51**, 821–830.

Skotheim, J. M. & Mahadevan, L. 2004 Soft lubrication. *Phys. Rev. Lett.* **92**, 245509.

Skotheim, J. M. & Mahadevan, L. 2005 Soft lubrication: the elastohydrodynamics of non-conforming and conforming contacts. *Phys. Fluids* **17**, 092101.

Sugiyama, K. & Sbragaglia, M. 2008 Linear shear flow past a hemispherical droplet adhering to a solid surface. *J. Engng Math.* **62**, 45–50.

Takemura, F. 2004 Migration velocities of spherical solid particles near a vertical wall for Reynolds number from 0.1 to 0.5. *Phys. Fluids* **16**, 204–207.

Takemura, F., Magnaudet, J. & Dimitrakopoulos, P. 2009 Migration and deformation of bubbles rising in a wall-bounded shear flow at finite Reynolds number. *J. Fluid Mech.* **634**, 463–486.

Takemura, F., Takagi, S., Magnaudet, J. & Matsumoto, Y. 2002 Drag and lift force on a bubble rising near a vertical wall in a viscous liquid. *J. Fluid Mech.* **461**, 277–300.

Uijttewaal, W. S. J. & Nijhof, E. J. 1995 The motion of a droplet subjected to linear shear flow including the presence of a plane wall. *J. Fluid Mech.* **302**, 45–63.

Uijttewaal, W. S. J., Nijhof, E. J. & Heethaar, R. M. 1993 Droplet migration, deformation, and orientation in the presence of a plane wall: a numerical study compared with analytical theories. *Phys. Fluids* A **5**, 819–825.

Urzay, J., Smith, S. G. L. & Glover, B. J. 2007 The elastohydrodynamic force on a sphere near a soft wall. *Phys. Fluids* **19**, 103–106.

Vasseur, P. & Cox, R. G. 1976 The lateral migration of a spherical particle in two-dimensional shear flows. *J. Fluid Mech.* **78**, 385–413.

Vasseur, P. & Cox, R. G. 1977 The lateral migration of spherical particles sedimenting in a stagnant bounded fluid. *J. Fluid Mech.* **80**, 561–591.

Wang, Y. & Dimitrakopoulos, P. 2006 A three-dimensional spectral boundary element algorithm for interfacial dynamics in Stokes flow. *Phys. Fluids* **18**, 082106.